Oxidation catalysis on Pt and Au : complexity of simple chemistry

Spronsen, M.A. van

Chapter 3

Oxidation of Pt(111), the effect of temperature and pressure studied with STM and XPS

3.1 Introduction

In the previous chapter, I presented high-pressure STM experiments that showed two different surface oxides that formed while the Pt(111) surface was exposed to high-pressure (1–5 bar) and high-temperature (437–538 K) conditions. The spoked-wheel oxide was stable from 1 to 5 bar, while the lifted-row oxide was only observed above ∼2 bar.

In this chapter, several supporting experiments will be discussed that deepen the insight into these surface oxides. All these experiments started similar to the experiments described in the previous chapter: a well-prepared Pt(111) surface was exposed to high pressure in the reactor also holding the STM. During this exposure, the surface was inspected with STM. In the first experiments, I have explored the influence of the kinetics on these oxides by exposing the Pt(111) surface to similar conditions but at lower temperatures, between room temperature and ∼320 K. These experiments show that similar structural features were formed, but without being ordered on a large scale.

A second set of experiments essentially started after the surface oxide was formed on the Pt(111) surface in the reactor cell. After high-pressure, high-temperature exposure, the vacuum stability was tested by evacuating the reactor. The results indicated that the spoked-wheel and lifted-row structures were not stable without the presence of the high O_2 pressure. After evacuation, a lower estimate of the O coverage under high-pressure conditions was determined with XPS performed under UHV conditions. This estimate was 0.88 ML, which agreed well with the formation of a single layer, surface oxide as presented in the model in Chapter 2.

3.2 Experimental

The in situ STM experiments were very similar in approach to those described in the previous chapter. The high-pressure STM experiments were performed in the ReactorSTM. Details about this system were described in Chapter 2. Also for the experimental details of the sample preparation, the used gases, and the STM experiments, the reader is referred to Chapter 2. In the first set of experiments, the Pt(111) surface was exposed to high pressure of O_2, but at lower temperature. The experiments probing the vacuum stability were performed in the ReactorSTM after forming the surface oxide under high pressure and high temperature by evacuating the reactor. These experiments were concluded with UHV XPS measurements. The XPS measurements were repeated at various temperatures to study the temperature stability of the formed surface oxides. All XP spectra were collected in UHV, but without exposing the sample to air. We used Al Kα radiation[1], for which we operated the anode at a potential of 14.1 kV. Emitted photoelectons were detected with a hemispherical analyzer[2] equipped with a collimator aperture to bring the spot size down to ∼8 mm. The detector was operated with a slit size of 4.0 mm and the electrostatic lenses at 3:1 mode, reducing the spot size further to ∼1.3 mm. The sample was facing the detector, with the X-ray beam impinging under an angle of 55° with respect to the surface normal.

[1] VG XR3E2, non-monochromatic
[2] VG Clam2/1VU, 100 mm radius

To ensure that the inspected area coincided with that exposed in the reactor, the ring-shaped imprint of the fluoroelastomer was used, on which a strong F peak could be discerned. Importantly, the center of the sample did not show any F contamination before or after the high-pressure experiments.

The energy range of interest, around the O 1s and Pt $4p_{3/2}$ peaks, was probed with a constant analyzer energy (25 V). The binding energies were calibrated against the known energy of the Pt $4p_{3/2}$ peak of 519.5(3) eV [93]. After calibration, the spectra were corrected by subtracting a linear background. The XP peaks were fitted with a Doniach-Šunjić function [94] convoluted with a Gaussian, requiring the following fitting parameters: binding energy, intensity, Lorentzian line width, Gaussian line width, and asymmetry factor. For the temperature-dependent XPS experiments, a simpler procedure was followed, consisting of subtraction of a constant background and normalization to the maximum Pt $4p_{3/2}$ intensity. This was followed by fitting the O 1s peaks with a Gaussian function.

3.3 Results

3.3.1 Exposure at lower temperature

To investigate the kinetics of the Pt(111) surface oxidation, experiments in the ReactorSTM were repeated at lower temperatures (327–328 K and ∼291 K) at an O_2 partial pressure of 1.0 bar. These experiments did not lead to large-scale ordered structures. This absence cannot be attributed to a lower resolution, as could have been caused by a blunter tip. The acquired STM images all showed subnanometer features as illustrated in Figure 3.1. These features showed the strongest contrast at very low bias voltages, between 20 and 50 mV, similar to the STM images described in the previous chapter.

Careful inspection revealed that the STM images obtained at lower temperatures at high O_2 pressure have recurring structural motifs. These patterns hinted at the formation of similar structures to those observed at elevated temperature. The predominant structure observed in the STM images (Figure 3.1a) at low-temperature exposure was a pattern of rows. The rows are indicated in the lower right panel of Figure 3.1a (annotated replica of the upper right panel). The periodicity of these rows was 0.49±0.02 nm and matched that of the lifted-row structure observed at high-pressure O_2 exposure, which was 0.46±0.01 nm. Both also corresponded well with $\sqrt{3}$ times the Pt(111) lattice constant, which is 0.48 nm.

A second observed structure was a triangular unit, the structural element of the spoked wheels, observed in several STM micrographs (Figure 3.1b) at 327–328 K. The small panels of Figure 3.1b show two duplicates of an enlarged region, in which a triangular shape was recognizable. This shape is depicted in blue in the lower right panel. Furthermore, the STM image contained many atomic features of various shapes. These features were true atomic shapes and did not originate from scan vibrations.

Finally, a third returning structure is shown in Figure 3.1c. In this STM image, many isolated clusters could be seen. Several of these clusters were analyzed as indicated in the lower right panel (annotated replica of the upper right panel). The average

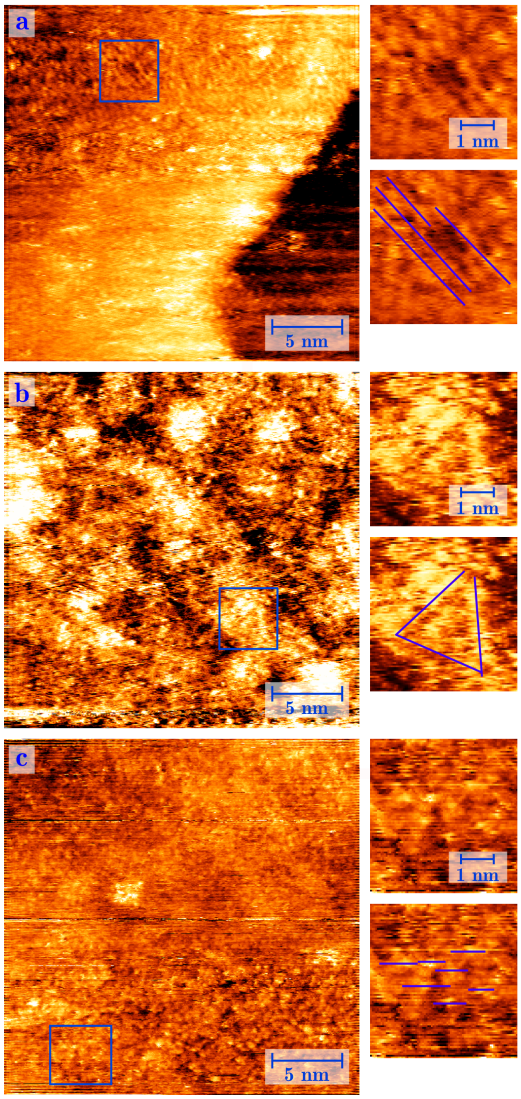

Figure 3.1: Several STM images (25×25 nm^2), shown together with enlarged regions, measured at 327–328 K at an O_2 pressure of 1.0 bar. Several structural features could be discerned that hinted at the formation of disordered versions of the ordered high-pressure structures found at higher temperatures (Chapter 2): rows (a, 1226 s exposure to O_2, $U_{bias} = -0.05$ V, $\overline{I_{tunnel}} = 0.48$ nA, $t_{image} = 9.9$ s), triangles (b, 843 s exposure to O_2, $U_{bias} = -0.02$ V, $\overline{I_{tunnel}} = -0.66$ nA, $t_{image} = 8.5$ s), and clusters (c, 2858 s exposure to O_2, $U_{bias} = 0.04$ V, $\overline{I_{tunnel}} = -1.19$ nA, $t_{image} = 15.5$ s). Nonlinear filtering was applied to remove some interference. Furthermore, the right panels of (b) have a nonlinear adaptive color scale to enhance contrast.

height between the top of the cluster and its surrounding minima was 0.06±0.02 nm (at a bias of 0.04 V). Although this value was not fully independent of bias voltage, the variations were small and all values were well below the Pt(111)-step height of 0.23 nm (SI, Table 3.2). The average estimated full width at half maximum (FWHM) was 0.32±0.04 nm. The FWHM of these clusters agreed well with the measured lattice constant of the spoked-wheel structure.

3.3.2 Evacuation experiments

To test the adsorption strength of the O atoms involved in these structures, we performed a series of experiments in which we evacuated the reactor after having formed the oxygen-rich structures in situ at high O_2 pressures, while the surface was continuously imaged with STM. The decrease in pressure was rapid and the pressure reached the (U)HV-regime within minutes, at which point the STM imaging was resumed. At the same time, heating of the surface was stopped and the sample was allowed to cool down.

The results obtained are summarized in Figure 3.2. The stable structures formed at 1.0 and 5.0 bar O_2 are illustrated by the STM images in Figures 3.2a and c, respectively. In both images the spoked-wheel oxide can be distinguished. In addition, the higher-pressure exposure resulted in a large fraction of the surface covered with the lifted-row structure. After growth, the reactor was evacuated and two representative STM images are shown in Figures 3.2b and d. They show that both well-ordered structures were unstable in the absence of the O_2 atmosphere. However, some hints of the remaining structures could still be distinguished. Some of these vague structures are highlighted in Figure 3.2b'.

3.3.3 XPS measurements

Coverage estimate

To estimate the O coverage, we performed UHV XPS measurements. The XPS measurements were expected to give a lower estimate for the O coverage, because the oxygen-rich structures were modified somewhat after lowering the O_2 pressure (see Section 3.3.2), which we associate with the desorption (or reaction) of some of the O atoms in these structures.

In order to reliably convert the XPS intensities into O coverages, we used the p(2×2)-O chemisorption structure as reference system. The XP spectrum of this reference structure is shown in Figure 3.3a. It was created by exposing a well-cleaned Pt(111) sample to a total O_2 dose of 400 L (one langmuir, L, is defined as 1×10^{-6} Torr×s) at room temperature. This exposure resulted in a well-known, saturated chemisorption structure. This structure has a (2×2) periodicity and a coverage of 0.25 ML [30, 31, 69–71]. We found the O 1s binding energy at 528.5 eV, which we assigned to chemisorbed O on the metallic Pt(111) surface. This is approximately one eV lower than usually found for chemisorbed O on Pt, as can be seen in Table 3.3, SI. In addition, the table shows that the spread in binding energies, reported in literature, is considerable. This spread could be due to differences in the employed calibration for the binding energy.

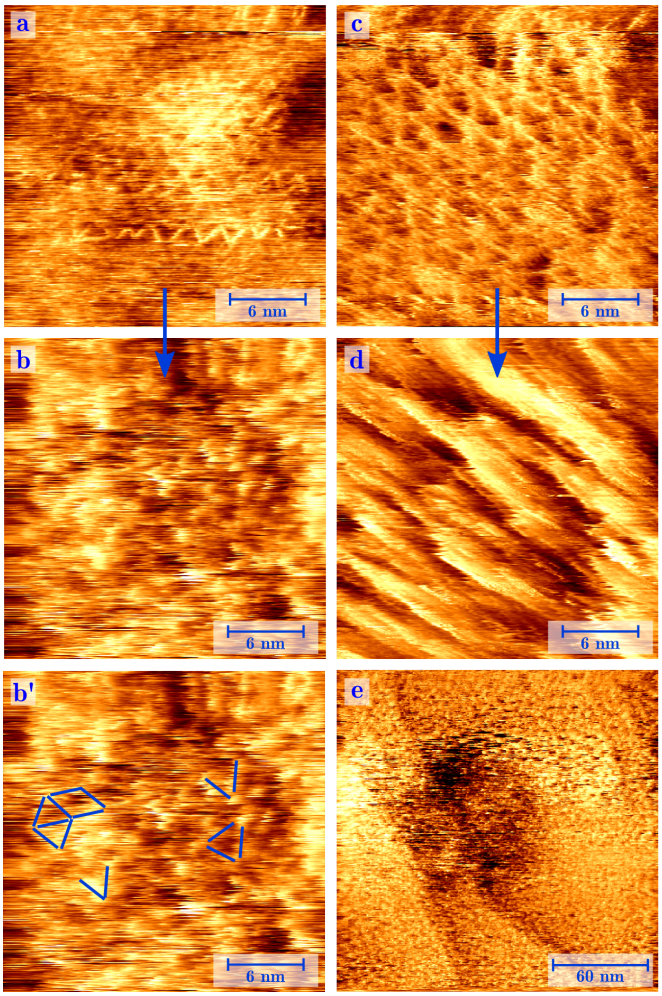

Figure 3.2: STM images obtained in situ, while oxidizing the surface (a and c) and after this high-pressure exposure, in high vacuum on a cooling sample (b, b', d, e). (a), surface mainly covered with spoked wheels, $p_{O_2} = 1.0$ bar, $T_{sample} = 529$ K, $t_{exposure} = 2715$ s (25×25 nm^2, $U_{bias} = 0.05$ V, $\overline{I_{tunnel}} = -2.66$ nA, $t_{image} = 17.8$ s). (b), disordered structure, obtained 3436 s after evacuation of (a), $T_{sample} = 336$ K (25×25 nm^2, $U_{bias} = 0.05$ V, $\overline{I_{tunnel}} = -0.48$ nA, $t_{image} = 17.8$ s). (b)' shows the same STM image as (b), highlighting several elements that hint at residues of the spoked-wheel structure. (c), mixture of spoked wheels and lifted rows formed at $p_{O_2} = 5.0$ bar, $T_{sample} = 538$ K, $t_{exposure} = 9728$ s, (25×25 nm^2, $U_{bias} = 0.1$ V, $\overline{I_{tunnel}} = -0.95$ nA, $t_{image} = 15.1$ s). (d), 2113 s after evacuation of (c), vague row pattern still discernible and many steps following the rows, $T_{sample} = 353$ K (25×25 nm^2, $U_{bias} = 0.1$ V, $\overline{I_{tunnel}} = -0.71$ nA, $t_{image} = 18.3$ s). (e) 4284 s after evacuation of (a), the surface is susceptible to tip-induced restructuring indicated by a changed morphology in the center of the STM image, $T_{sample} = 331$ K (200×200 nm^2, $U_{bias} = -0.03$ V, $\overline{I_{tunnel}} = 0.26$ nA, $t_{image} = 75.8$ s).

The XP spectrum of chemisorbed O was compared with the graph (Figure 3.3b) obtained after exposing a clean sample to high O_2 pressure and temperature (1.0 bar O_2, 441–444 K, 60 minutes). While exposing the sample to these conditions, it was confirmed with STM that the spoked-wheel structure had formed. After forming the structure, XPS measurements were performed. The differences were evident: the O 1s intensity had strongly increased and shifted from 528.5 eV to 530.7 eV. The higher binding energy agreed well with the values found for oxidized Pt (see SI, Table 3.4). In this table, a clear trend is missing, although PtO_2 seems to be generally lower in binding energy than the surface oxides and PtO. Our shift to higher binding energies matched with the comparison of binding energies of surface oxides with chemisorbed oxygen found in literature (SI, Table 3.3 and 3.4), although it disagreed with the study by Miller et al. on Pt(111) [39].

The FWHM of the new O 1s peak was estimated at 2.4 eV. XPS peaks with similar widths were both attributed to a single O state [32, 95] or to a pair of states [35]. Based on the shape and width of the O 1s peak and the resolution of our XPS system, we associate the peak with a single O state, although we cannot fully exclude the possibility of closely separated states.

The resulting increase in O 1s signal from the p(2×2) structure to the surface oxide was a factor 3.5. This corresponds to an O coverage of 0.88 ML. Based on variations in the fitting results, we expected the uncertainty on the O coverage to be ± 0.1 ML. Although the XPS-derived O coverage was a lower estimate, the measurement suggested that the surface oxide had a thickness of a single layer.

Temperature dependence

A second XPS study focused on the temperature dependence of the spoked-wheel structure. The XP spectra were taken at temperatures between 432 and 963 K. The results are presented in Figure 3.4. The spectrum labeled "1056 K" was collected at lower temperatures after annealing briefly to 1056 K. The change in O coverage plotted as function of temperature is depicted in Figure 3.4b. The graph shows a constant, almost linear decrease in O coverage with increasing temperature. After annealing to 1056 K, the O coverage was on the level of the experimental noise, as is indicated by the large error margin for that temperature. Although the oxygen-rich structures were starting to release O between 432 and 564 K, some O was still on the surface at 963 K. This is either above or on the higher edge of O_2 desorption from the Pt(111), Pt(100), and Pt(110) surfaces [30–34, 36, 62, 96–100]. The increased stability can be a result of the roughness on the surface [60], but it could also indicate subsurface O [60, 88].

In the first (black) spectrum in Figure 3.4, some intensity was observed around 535 eV. It was not clear whether this was a real peak, noise, or a change in background. This was not observed in the higher-resolution spectrum of Figure 3.3b. Furthermore, it would not be easy to account for a binding energy shift to 535 eV [101].

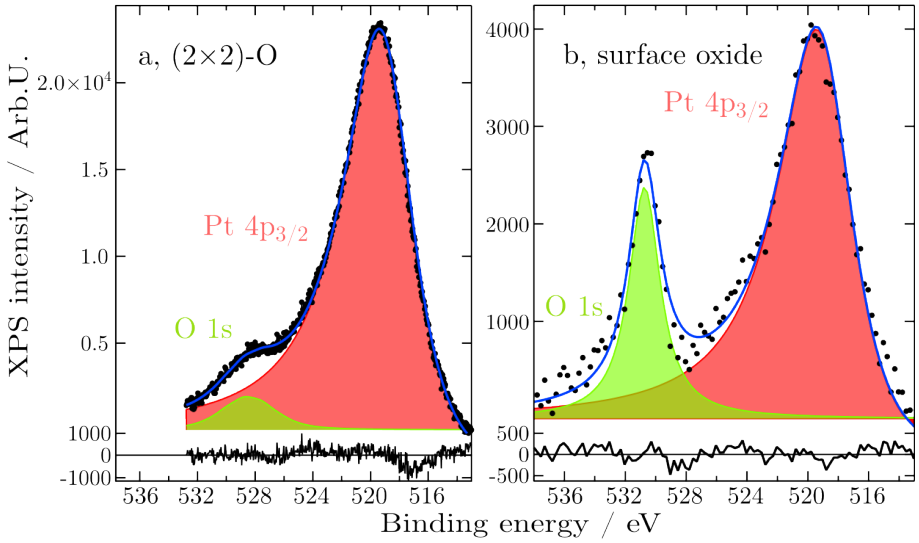

Figure 3.3: XP spectra collected after exposure of a clean Pt(111) sample to 400 L O_2 at room temperature (a) and to 1.0 bar O_2 at 441–444 K for 60 minutes (b). Spectra were fitted with a Doniach-Šunjić function [94] convoluted with a Gaussian: O 1s (green) and Pt $4p_{3/2}$ (pink). Lower panels show the fitting error. To obtain a good fit, the Pt $4p_{3/2}$ peak required considerable asymmetry in both spectra.

3.4 Discussion

3.4.1 Effect of pressure and formation temperature

Exposure of the Pt(111) surface to a high O_2 pressure (1.0 bar) at lower temperature (327–328 K and ∼291 K), did not lead to large-scale ordered structures. At these lower-temperature conditions, thermodynamics predicts an even higher driving force to create oxygen-rich structures. This seems to contradict the observations and, hence, two possibilities remain. The first one is that the disordered structures that were observed contained more O than the surface oxide. In this case, the structures would have to be disordered multilayers or contain subsurface O. The second possibility is that the formation of both surface oxides was kinetically hindered at lower temperatures. This seems to be confirmed by the observation of the basic structural elements, lifted rows and triangles, that are the building block for the ordered, higher temperature structures. The limiting step can either be the rearrangement of the Pt atoms on a larger scale or the dissociation of O_2. Similar observations were made on Pt(110) after oxidation at lower temperature [62].

The main extra feature observed at lower temperature were clusters with a diameter of 0.32±0.04 nm. The clusters' apparent height was much smaller than a monoatomic step and was relatively unaffected by changes in the sample bias. Therefore, we

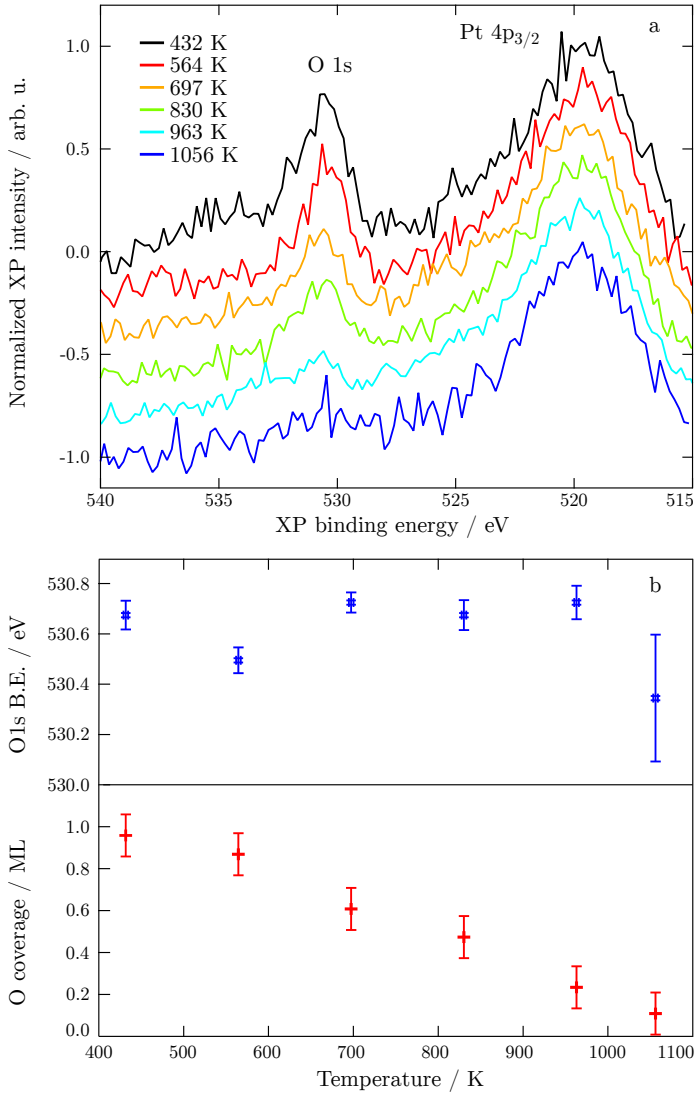

Figure 3.4: (a), XP spectra measured at different sample temperatures after high-pressure and high-temperature exposure (1.0 bar O_2, 433–438 K, 53 minutes, after which the sample was allowed to cool to 332 K in 33 minutes at the same O_2 pressure). (b), temperature dependence of the fitted binding energies of the O 1s peak (blue; upper scale) and the integrated O 1s peak areas (red; lower scale). The error bars were based on the uncertainty of the binding energy in the fit and on the variation of coverage with changes in fitting parameters. The latter was estimated to be ± 0.1 ML.

propose that these clusters were single PtO_x units, buckled out of the surface. It could be the building block of both the spoked-wheel and the lifted-row surface oxides. Similar clusters were previously observed [33] and DFT showed that units consisting of a Pt atom surrounded by three O atoms were stable structures [61].

3.4.2 Thermal decomposition and stability with respect to chemisorbed O

After evacuation, the imaged surface appeared very rough and the STM imaging much noisier. This increase in noise in (U)HV conditions compared to high-pressure conditions seems counterintuitive. To explain this, we propose that both structures were thermodynamically unstable without the high O_2 pressure. These unstable structures were releasing O_2, which increased the mobility of Pt atoms. This mobility was responsible for the observed noise in the tunneling current, which affected the quality of the STM images and was observed as single-scan-line noise. Under these conditions, we saw evidence for a significant influence of the tip on the surface structure, possibly via its interaction with the mobile Pt atoms, or by enhancing the rate of departure of O atoms. For example, the STM image of Figure 3.2e was recorded after the central region of the image had been scanned several times, and it showed that this region had suffered a loss of material with respect to its surroundings, while the stripiness indicates significant mobility in or on the depressed region.

There was a clear difference between the surface obtained after evacuation, starting from 1.0 bar O_2 and that from 5.0 bar O_2. After exposure to 1.0 bar O_2 and subsequent evacuation, the terraces exhibited a noisy two-level structure (Figure 3.2e) that was less well organized than the two-level pattern of Figure 2.1b. The STM image following evacuation after exposure to 5.0 bar O_2 showed that the surface tried to avoid steps perpendicular to the lifted oxide rows (Figure 3.2d). The observed step configurations are reminiscent of those on the missing-row-reconstructed Pt(110) surface [25, 26].

The binding energies are remarkably constant as O_2 is desorbing from the surface (Figure 3.4b). Only the last spectrum, taken after annealing to 1056 K, shows a shift to lower binding energies, but this could be completely related to the noise on the measurement, as is indicated by the large error margin for that temperature. The absence of a shift is interesting; it can be explained by a reduction of the surface area covered with this oxygen-rich structures, while an increasing portion of the surface becomes empty, metallic Pt. Alternatively, the surface oxide could have decomposed into a chemisorption structure, but only if that was rather different from the p(2×2)-O structure, as it had the same O 1s binding energy as the surface oxide. It could be that such an alternative chemisorption structure is related to the oxygen-induced roughening. The latter explanation is supported by the work of Parkinson et al., in which they observed a (2×2) LEED pattern during decomposition of oxygen-rich structures created by atomic O exposure of the Pt(111) surface [35]. The (2×2) state, observed with LEED, had an O 1s binding energy of 530.8 eV, very close to our reported values.

All results strongly suggested that the oxygen-rich structures were unstable upon evacuation. However, the loss of oxygen was kinetically delayed within the time

scale of our experiment. In the STM experiments, no structures with lower oxygen coverage, such as the vacuum-stable surface oxide [33], were observed. In addition, the noise characteristics of the tunneling current gave also the impression that the surface remained oxidized.

3.4.3 Tunnel-gap resistance and tip effects

The tip-sample interaction depends strongly on the tip-sample distance, which, in turn, is related sensitively to the resistance of the tunneling gap. The usual gap resistance[3] is around 10 GΩ when the sample is a clean, metallic surface. In contrast, a gap resistance[4] of 20 MΩ was found to result in the highest resolution on the surface oxides. The surprising aspect was that bias voltages of approximately 20–50 mV were used to image the surface oxides. This implied that the surface oxides had no or a very small band gap. This contradicted with an STM finding of a 2D surface oxide and disordered oxide clusters on the Pt(110) surface, which did show a significant band gap of >1 V [62].

Pt oxides do not behave like the typical wide-band-gap oxides, such as SiO_2 and Al_2O_3. For Pt oxides, the band gaps are relatively small and these oxides are generally considered to be semiconductors. For example, experimental values for the band gap of crystalline PtO_2 were 1.8 eV [102] and 2.5 eV [103]. The band gap was found to be significantly lower for amorphous PtO_2 (1.2–1.3 eV)[75, 77]. For Pt oxides with a lower oxidation state, the band gap is also reduced, although previous results are conflicting. PtO was found to be a metal [79] or a semiconductor [49] with low conductivity [50] in different experimental studies. However, the most recent DFT calculations employing hybrid functionals gave a band gap of 0.9 eV [104, 105]. The decrease in band gap with decreasing oxygen content was also observed when PtO was compared with the hypothetical Pt_8O_7, which had a 0.3 eV lower band gap. Furthermore, Pt_3O_4 was suggested to be metallic in nature due to the presence of Pt-Pt bonds in the crystal structure [106], which, however, still requires experimental confirmation. Finally, metallic behavior was also reported for amorphous PtO_x, with x between 1 and 2.

Our STM experiments showed that the observed surface oxides had a minute or nonexisting band gap. The lack of a band gap can be explained in two steps. Firstly, the 1D oxide chains in the proposed model are structurally more related to the lower-band-gap oxides, PtO and Pt_3O_4 than α-PtO_2 (vide supra). In addition, the Pt atoms in the 1D oxide chains are closely spaced with the Pt atoms not directly involved in the surface oxide and, possibly, these two kinds of Pt atoms can sufficiently bind to eliminate the band gap.

Alternatively, the absence of a band gap can be rationalized by a fractional oxidation state. Oxidation states of Pt oxides deviate strongly from the formal oxidation states of Pt^{2+} and Pt^{4+} and have a significant covalent character. This has been shown consistently with DFT calculations [57, 61, 64, 104–106] and can also be expected for the surface oxides. This fractional oxidation state results in partial occupation of the highest-energy d-orbital. This orbital is the $d_{x^2-y^2}$ orbital for the square planar PtO_4

[3] $U_{bias} \approx 1$ V and $I_{tunnel} \approx 100$ pA
[4] $U_{bias} \approx 20$ mV and $I_{tunnel} \approx 1$ nA

units according to crystal field theory [107]. This orbital is empty for d8-configurations, like Pt^{2+}. Partial filling of the $d_{x^2-y^2}$ orbital could as a consequence decrease the Pt-O bond strength, because this orbital could be antibonding with respect to those bonds. Finally, it is possible that the lack of band gap was because of the defects present in these surface oxides. This defects are abundant and clearly discernible in all STM images presented in this work.

Imaging at low values for the tunneling gap resistance had as main drawback that the strong tip-sample interaction resulted in STM artefacts. One example of an STM tip artefact is visible in Figure 3.2e. These effects were generally observed under less-oxidizing conditions and were all destructive in nature, resulting in a rough surface without discernible atomic structure. All STM observations on the high-pressure oxide structures were unrelated to STM-tip effects. This was carefully checked by moving the scan region to a fresh area or by zooming out and comparing the inner region of the STM image with the outer parts (Figure 3.2e).

3.4.4 Stability with respect to α-PtO_2

Equally important as the spoked-wheel and lifted-row oxides, discovered here, is the structure we did *not* observe, i.e., α-PtO_2. This directly conflicts with the conclusions of two SXRD studies that probed the Pt(111) surface under similar conditions [37, 38]. The conclusions in these studies were strongly based on the in-plane diffraction spots, which indicated a hexagonal overlayer with a lattice constant close to that of α-PtO_2. However, the spoked-wheel oxide would give similar in-plane hexagonal diffraction spots. In the SXRD results, the difference would be in the "crystal" truncation rods of the oxide, to which only a model was fitted based on α-PtO_2. Furthermore, both studies found a hexagonal unit cell parallel to the Pt(111) unit cell. This contradicted both experimental and theoretical studies that showed a 30°-rotated α-PtO_2 layer [29, 54, 108, 109]. The oxide layer had a $(\sqrt{3}\times\sqrt{3})$ unit cell on a (2×2) Pt(111) unit cell to minimize the misfit between the structures. We conclude that the SXRD observations actually support the identification of the spoked-wheel oxide on the Pt(111) surface at high O_2 pressures.

Another scenario would be that α-PtO_2 was still formed during the SXRD studies. The discrepancy between the SXRD and STM studies could then be explained by a kinetically hindered formation of α-PtO_2. This hypothesis is supported by a calculated phase diagrams showing that α-PtO_2 should be the stable phase under these experimental conditions [29, 54, 110]. In this case, the observed spoked-wheel and lifted-row oxides were only metastable with respect to α-PtO_2. This kinetic limitation that must have been at play in this scenario can hardly be attributed to a lack of mobility. The Pt atoms do not have to move significantly more to form a layer of α-PtO_2(0001) than to form the spoked-wheel and lifted-row surface oxides. Second, we observed an enormous mobility, which can be seen when Figure 2.1a and b are compared. Therefore, any kinetic limitation should be related to either O_2 dissociation or O diffusion into subsurface sites. The differences in O-related kinetics cannot be explained by a difference in temperature between the STM and the SXRD experiments, because similar temperatures were employed in all studies. The difference

can be explained by X-ray-induced formation of O_3. This was already identified by Ackermann and others [38, 59] as a possible artefact in synchrotron-radiation-based experiments. Ozone was observed to strongly oxidize Pt under UHV conditions [34].

In a near-ambient-pressure XPS study, temperature was the important parameter. Only at 720 K, the formation of α-PtO_2 was observed, below this temperature only the "4O" phase was found. The latter phase was structurally almost identical to the proposed model of the lifted-row oxide, although it is unclear whether XPS or XAS would be able to differentiate between the spoked-wheel and the lifted-row oxides.

To conclude, it remains uncertain whether the surface oxides in this work are the thermodynamically most stable stable phases. They could have been 'stabilized' by the kinetic limitation to form α-PtO_2. More important than thermodynamic stability is the question of stability under catalytic conditions.

3.4.5 Implications for catalysis

The surface oxides observed in this study were unstable in vacuum. From the instability in the evacuation experiments, it can be concluded that these oxides contain O atoms that are loosely bound and therefore highly reactive. Although no true distinction between desorption and reaction with background gas could be made, both cases would lead to the conclusion of the presence of highly reactive O atoms. For the spoked-wheel oxide, an interesting question to answer is which O atoms are more reactive. Are those the O atoms forming the Pt oxide stripes or are those the chemisorbed O atoms, which in turn can feel a strong repulsion from the Pt oxide spokes?

The oxidation-induced roughness was very similar to the observed roughness under CO oxidation conditions in an O_2-rich flow. Under these conditions, a higher reactivity was found [111]. Both the roughness and the higher reactivity phase can very well be explained by the formation of a single layer of the spoked-wheel oxide. In addition, these surface oxides were very recently also identified as the stable phase under NO oxidation conditions. These experiments are not described in this PhD thesis and will be reported in a separate publication.

To translate the results obtained on a Pt(111) model catalyst to real and complex catalysts, one important point to address is the effect of nanoconfinement. This confinement is a direct consequence of the use of nanoparticles as catalysts. The sizes of their (111) facets will be on the same order as the diameter of a spoked wheel for the smallest particles. This could make the spoked-wheel oxide less stable. On the other hand, nanoparticles may have less difficulty to relieve the strain induced by the surface oxide than an extended single crystal. To clarify this point, in situ experiments yielding atomic resolution on particles possibly aided by DFT calculations will be needed.

3.5 Summary and conclusions

In summary, in this chapter we have found the following:

1. At high O_2 pressures, but lower temperatures, surface oxides were formed on Pt(111) that did not show ordered structures, although some structural motifs like rows

and triangles were observed, similar to the basic structures of the spoked-wheel and lifted-row oxides that were formed at higher temperatures, reported in the previous chapter. In addition, many small clusters having a width of 0.31±0.04 nm were identified that could be clusters of a single Pt atom surrounded by three O atoms [61].

2. Evacuation experiments showed that these surface oxides were not stable without the presence of the high O_2 pressure. This resulted in slowly disappearing structures.
3. XPS measurements in UHV after forming the surface oxides in situ, indicated an O coverage of 0.88 ML. This agreed very well with the model of single-layer surface oxides.

Based on these findings, our main conclusions can be stated as follows:

1. On the Pt(111) surface, the stability of the surface oxides depended both on a high chemical potential as driving force to form and possibly a kinetic limitation against the formation of a bulk-like oxide layer. The surface oxides dictated the nature and reactivity of O atoms on the surface.
2. UHV studies cannot be used a priori to make Pt oxides that represent the surface structure under catalytic conditions. The surface oxides were observed in combination with a large-scale roughness. No UHV study to date has been able to capture both aspects with oxidation using stronger oxidants.
3. One must interpret the data of in situ studies with care. This new type of research relies more strongly on a single experimental technique, compared to traditional UHV surface science work, in which it is more customary to combine several experimental tools. For the oxidation of Pt(111), a large apparent discrepancy was found between our STM work and earlier SXRD experiments [37, 38], which could be explained either by the limited range of the structural models considered for fitting the SXRD results or by the formation of α-PtO_2 as a result of the oxidizing nature of the X-ray-induced O_3 species.

Supplementary information – Oxidation of Pt(111)

Temperature calibration

In the current design of the sample holder and sample transfer system of the ReactorSTM [19], the thermocouple connections are not entirely consisting of thermocouple material. To make the transferable connections, gold-plated copper alloy connectors are used. Over these connectors, a temperature gradient will arise upon heating the sample. This gradient results in an erroneous temperature reading.

We performed a temperature calibration to quantify the error in the temperature measurement. To obtain the misreading, a second thermocouple was laser-spot welded directly to the sample and to a true K-type thermocouple UHV feedthrough. The temperature calibration was performed in two environments. One was the UHV environment used for sample cleaning and XPS measurements. The other one was with the sample mounted in the reactor and exposed to a mixture of O_2 and Ar (5:1, flow: 8 ml/min, p_{O_2}: 1.0, 2.66, and 5 bar). All results indicated that the true sample temperature was higher than the temperature measured via the standard thermocouple.

Figure 3.5 shows the results obtained when the sample was annealed in UHV with a sample voltage of 1 kV. The temperature errors are plotted such that they appear positive. The upper panel shows the total power needed to anneal the sample to a specific temperature. It shows that up to 670 K, the power scaled linearly with temperature. In this regime, the filament was not hot enough to emit electrons and the only source of heating was radiative. Above 670 K, a sample current was measured in the range of 2–10 mA originating from electron-beam (e-beam) heating by the filament. In this regime, the required total heating power was following a superlinear increase.

In the lower panel (Figure 3.5), the temperature error was plotted versus the true temperature. The error approached 200 K at a sample temperature of 1200 K and was showing linear dependence on the true temperature. However, the slope of the curve decreased by 30 % after e-beam heating started. The two resulting conversion formulae ensured an error in the temperature below 1 % for UHV annealing.

The temperature calibration of the sample in the reactor at high pressure is shown in Figure 3.6. In this case, the sample was solely heated by thermal radiation by the filament. The investigated temperature range was much smaller as it was limited by the degradation temperature of the fluor elastomer seal[5]. The figure illustrates that the error was strongly nonlinear. It increased linearly between 294 K and 425 K. The maximum error was 13.5 K at 425 K. Further heating resulted in a decreasing error. In fact, the smallest error (4–5 K) was measured at the highest temperature (530 K). Changing the absolute pressure at this temperature from 1.2 to 6.0 bar did not significantly influence the error. Although this temperature behavior was complex, its effect was small and with this calibration we estimate the error to be around 0.25 K for temperatures recorded in the high-pressure experiments.

In the discussed calibrations, long time intervals between data points were included in order to ensure thermal equilibrium. Deviation from thermal equilibrium, gave a time-dependent misreading. This error originates in different heating rates of various parts of the microscope. This effect was studied by making a single, sufficiently large step in the

[5] TM Kalrez® 7075 [40]

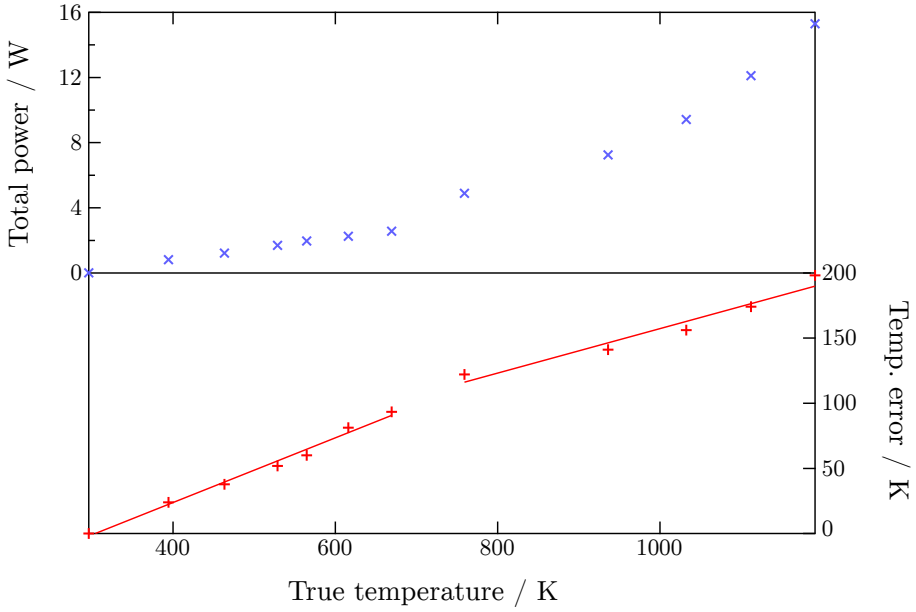

Figure 3.5: Calibration of the effect of the ReactorSTM's non-thermocouple connectors on the sample temperature, measured with a true K-type thermocouple. Sample is in the UHV environment with a sample-to-ground voltage of 1 kV. The upper panel shows the total heating power (sum of the power to heat the filament and the e-beam heating power on the sample) needed as a function of the true temperature, while the lower panel shows the underestimation by the regular temperature reading.

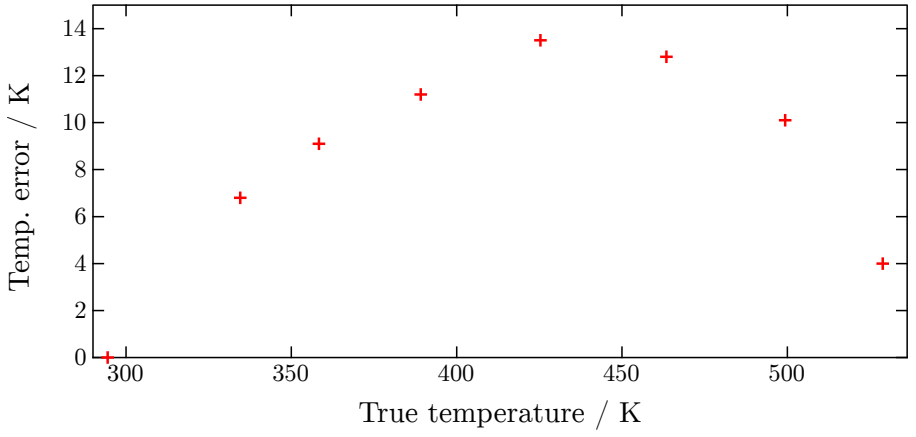

Figure 3.6: Temperature error versus the true sample temperature with the sample in the reactor at high pressure (p = 1.2 bar, O_2:Ar mixture of 5:1, flow of 10 ml/min), simulating the high-pressure experimental mixture. The data points were measured after the temperature error was stabilized.

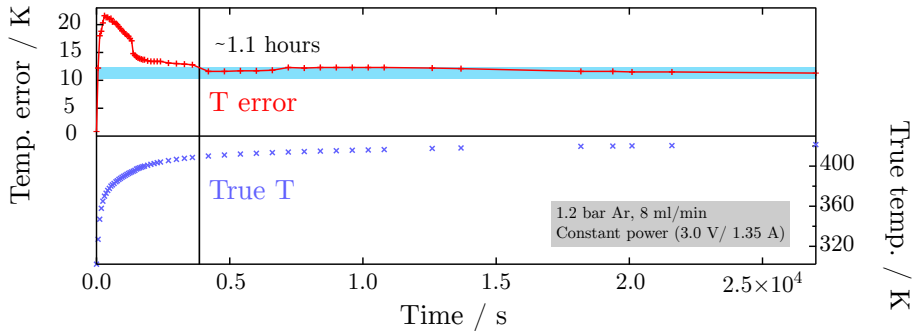

Figure 3.7: Time-dependent error in the temperature reading due to the fact that the microscope is out of thermal equilibrium after a step in the heating power. Upper panel shows the temperature error as a function of the time, while the lower panel shows the true temperature versus the time. The light blue band in the upper panel gives a ± 1 K interval around the final error found after a equilibration time of 7.5 hours.

heating power. After this step, the heating power was kept constant and the temperature error was recorded as a function of time. The results are depicted in Figure 3.7.

After the stepwise increase in power from 0 to 5.8 W, the error quickly increased to a maximum of 22 K after 300 s. After this maximum, the temperature error decreased to a value of 11.3 K after 7.5 hours. In spite of a very long equilibration time, the error is already within 1 K (light blue band, Figure 3.7) of the final value after 1.1 hours. This time interval is in the same order as needed for thermal drift in the STM to stabilize before starting the experiment. Therefore, all reported temperatures during the experiment were not affected by the time dependence of the temperature error.

LEED

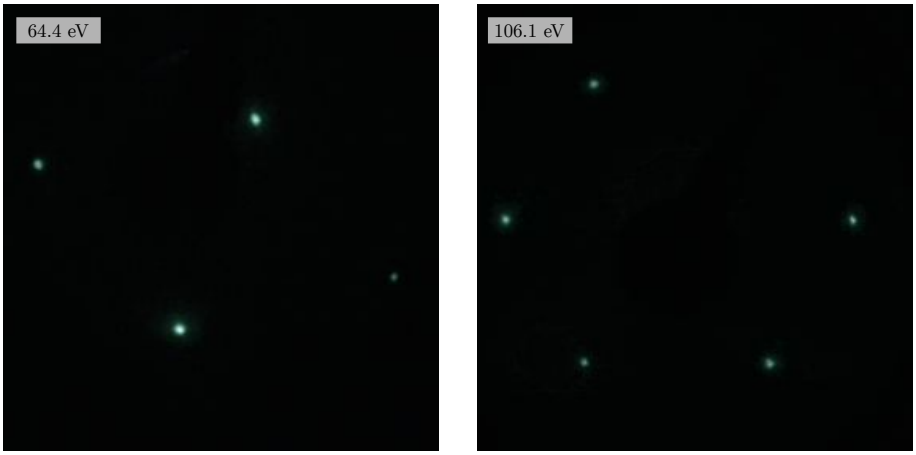

Figure 3.8: Two photographs of LEED patterns from a freshly prepared Pt(111) surface taken at an electron energy of 64.4 (left) and 106.1 eV (right).

Apparent height - spokes

The apparent height of the spokes of the spoked-wheel structure was measured at three different bias voltages (10–100 mV) with the same tip in the same experiment. The bias range was small due to the fact that low positive voltages were required to obtain atomic resolution of the spoked-wheel structure. The apparent height showed a small variation with bias voltage as present in Table 3.1, but the effect is very small with respect to the error bars.

A second measurement at 0.05 V in a different experiment showed much less height corrugation, i.e., 0.03±0.01 nm. This was only about one third of the corrugation that was found in the first measurement at the same bias voltage. Both experiments were performed with the same Pt/Ir tip, but the tip apex was altered between the experiments due to a crash in the surface. It showed that the apparent height was much more sensitive to the shape and/or state of the tip apex than to the applied tunneling bias voltage.

Apparent height - clusters

In the experiments at lower temperature (∼328 K and ∼291 K), clusters were observed while the surface was exposed to 1.0 bar O_2. The apparent height was measured at several different sample bias settings. The results are presented in Table 3.2.

Bias/V	App. height/nm	Stand. dev./nm
0.10	0.12	0.06
0.05	0.11	0.04
0.01	0.10	0.03
0.05	0.03	0.01

Table 3.1: Apparent height of the spokes of the spoked-wheel structure observed during the exposure of the Pt(111) surface to 1.0 bar O_2 at 529–537 K at three different sample bias voltages. The second measurement at 0.05 V was performed with the same STM tip, but in a separate experiment with, most likely, a different tip apex.

Bias/V	App. height/nm	Stand. dev./nm
0.69	0.09	0.02
0.04	0.06	0.02
-0.05	0.12	0.04

Table 3.2: Apparent height of clusters observed during the exposure of the Pt(111) surface to 1.0 bar O_2 at lower temperatures (327–328 K) at three different sample bias voltages.

Calculation of ideal O coverages

Spoked-wheel oxide

The (8×8) unit cell contains 4 Pt oxide spokes on the edges of the unit cell (sharing O atoms between two adjacent unit cells) and one spoke in the inside of the unit cell. Every spoke contains 7 Pt atoms with a PtO_2 stoichiometry, thus 14 O atoms. One O atom between spokes is shared, so the six corners reduce the number of O atoms with 6. This leads to:

$$\begin{aligned} 4\times14\times0.5&=28\\ 1\times14\times1&=14\\ 6\times-1&=-6 \qquad +\\ \hline &36 \text{ O atoms per unit cell} \end{aligned}$$

Additionally, 6 chemisorbed O atoms reside in the inner region of the triangle. So, the total number of O atoms is 48, 36+(2×6). In a (8×8) unit cell on the Pt(111) surface, 64 Pt atoms are located and this leads to $\frac{48}{64}$=0.75 ML.

Honeycomb oxide

One complete honeycomb (Figure 3.9) is described by a nonprimitive hexagonal unit cell, which spans the area of 3 (8×8) unit cells and contains 6 spokes on the unit

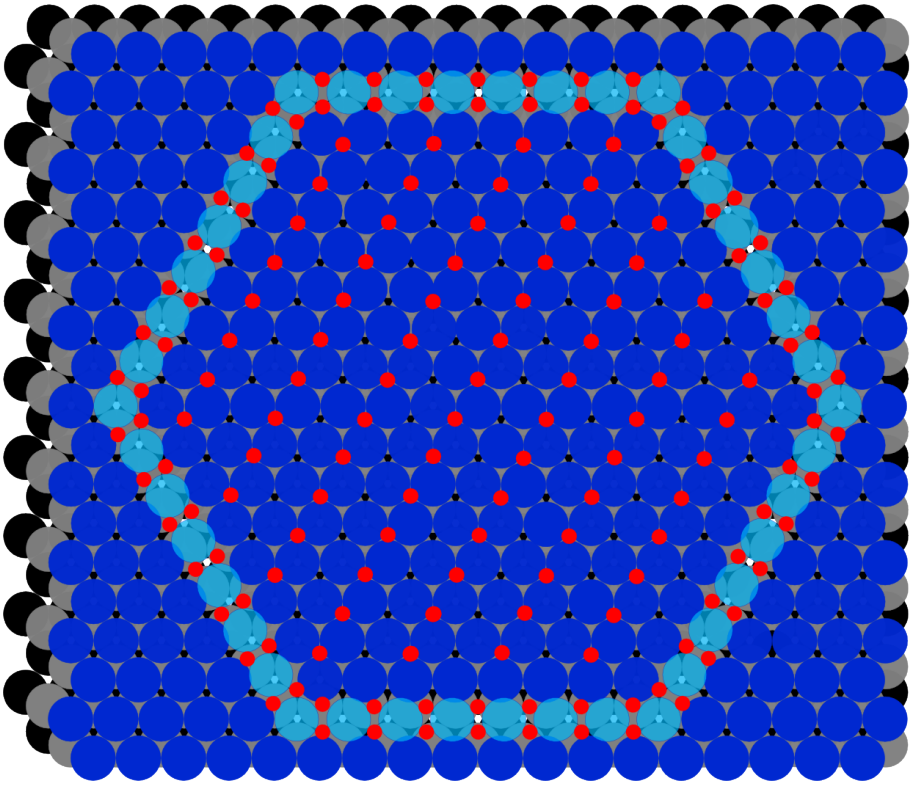

Figure 3.9: Ball model of the honeycomb-shaped surface oxide observed in Reference 33. Honeycomb's edges consist of the expanded Pt atoms (light blue), which are lifted from the surface plane (blue). In this model, the O (red) positions were deduced from literature [33, 61]. The inner region is covered with a p(1×2)-O chemisorption structure. The radii of the balls are based on the atomic radii of Pt and O.

cell's edges. Each spoke contains 7 expanded Pt atoms with PtO_2 stoichiometry. This equals to 42 O atoms. Counting the chemisorbed layer leads to an additional 74 O atoms. All O atoms together, it adds up to 116 O atoms and the total O coverage corresponds to $\frac{116}{3\times64}$ =0.60 ML.

This is lower than the experimental coverages of the honeycomb oxide obtained with temperature-programmed desorption (TPD) [33]. This could be attributed to formation of subsurface oxygen species or due to doubling of Pt oxide spokes.

Lifted-row oxide

The following calculation was based on the lifted-row oxide model with the (2×8) unit cell as depicted in Figure 2.9b. A calculation based on the (4×8) unit cell, would

lead to the same result. The lifted-row oxide holds one row of 7 expanded Pt atoms with a stoichiometry of PtO_2. This amounts to 14 O atoms. A (2×8) unit cell on a Pt(111) surface contains 16 Pt atoms. The total O coverage equals $\frac{14}{16}$=0.88 ML.

O 1s binding energy - references

O 1s B.E. / eV	Sample	Reference	Notes
529.4	Pt(111)	112	
529.5	Pt(531)	60	
529.55	Pt(332)	64	
529.7	Pt(111)	39	
529.7	Pt(110)	59	
529.75	Pt(111)	64	
529.8	Pt(111)	30	
530.2	Pt(111)	95	
530.8	Pt(111)	35	[1]
530.8	Pt(111)	32	
530.8	Pt(100)	32	

Table 3.3: O 1s binding energies of species attributed to chemisorbed O on Pt. [1]After decomposition of Pt oxide.

O 1s B.E. / eV	Assignment	Reference	Notes
529.5	surface oxide	39	Pt(111)
530.1	PtO_2	39	Pt(111)
530.2	PtO_2 on Pt	95	Pt(111)
530.3	PtO_2 (bulk)	95	Pt(111)
530.3	PtO_2	78	[1]
530.4	PtO_2	113	[2]
530.5	oxidic layer	35	[3]
530.6	PtO_{1+x}	74	[1]
530.6	PtO_2	74	[1]
530.8	surface oxide	60	Pt(531)
530.8	surface oxide	59	Pt(110)
531	PtO	[74]	[1], broad
531.4	PtO	[74]	[1]

Table 3.4: O 1s binding energies assigned to oxidized Pt.
[1] Sputtered Pt ox films.
[2] O_2 plasma of polycrystalline Pt film.
[3] Fitted with peaks at 530.8 eV (chem. O) and 530.2 eV (oxide).